

Article

Performance of a Solar-Driven Photocatalytic Membrane Reactor for Municipal Wastewater Treatment

Mirela Alina Constantin ¹, Lucian Alexandru Constantin ¹, Ioana Alexandra Ionescu ¹,
Cristina Mihaela Nicolescu ², Marius Bumbac ^{2,3} and Olga Tiron ^{1,*}

¹ National Research and Development Institute for Industrial Ecology-ECOIND, 57-73 Drumul Podu Dambovitei, District 6, 060652 Bucharest, Romania; alina.constantin@incdecoind.ro (M.A.C.); lucian.constantin@incdecoind.ro (L.A.C.); ioana.ionescu@incdecoind.ro (I.A.I.)

² Valahia University of Targoviste, Institute of Multidisciplinary Research for Science and Technology, 13 Aleea Sinaia, 130004 Targoviste, Romania; cristina.nicolescu@valahia.ro (C.M.N.); marius.bumbac@valahia.ro (M.B.)

³ Valahia University of Targoviste, Faculty of Science and Arts, 13 Aleea Sinaia, 130004 Targoviste, Romania

* Correspondence: olga.tiron@incdecoind.ro

Abstract: The increasing demand for efficient wastewater treatment technologies, driven by global population growth and industrialisation, highlights the necessity for advanced, reliable solutions. This study investigated the efficacy of a slurry photocatalytic membrane reactor (PMR) for the advanced removal of organic pollutants, quantified via chemical oxygen demand (COD), under natural and simulated solar light irradiation. Employing two variants of iron-doped titania as photocatalysts and a polysulfone-based polymeric membrane for the separation process, the investigation showcased COD removal efficiencies ranging from 66–85% under simulated solar light to 52–81% under natural sunlight over a 7 h irradiation period. The overall PMR system demonstrated COD removal efficiencies of 84–95%. The results confirmed the enhanced photocatalytic activity afforded by iron doping and establish solar-powered slurry PMRs as an effective, low-energy, and environmentally friendly alternative for the advanced treatment of municipal wastewater, with the research providing valuable insights into sustainable water management practices.

Keywords: PMR; solar light; wastewater; advanced treatment; photocatalysis; membrane processes



Citation: Constantin, M.A.; Constantin, L.A.; Ionescu, I.A.; Nicolescu, C.M.; Bumbac, M.; Tiron, O. Performance of a Solar-Driven Photocatalytic Membrane Reactor for Municipal Wastewater Treatment. *Processes* **2024**, *12*, 617. <https://doi.org/10.3390/pr12030617>

Academic Editors: Jasmina Dostanic and Davor Lončarević

Received: 7 February 2024

Revised: 15 March 2024

Accepted: 18 March 2024

Published: 20 March 2024



Copyright: © 2024 by the authors. Licensee MDPI, Basel, Switzerland. This article is an open access article distributed under the terms and conditions of the Creative Commons Attribution (CC BY) license (<https://creativecommons.org/licenses/by/4.0/>).

1. Introduction

One of the present challenges in the field of water/wastewater treatment is represented by the development of low-cost advanced treatment methods able to degrade/remove hazardous, non-biodegradable pollutants.

Most conventional municipal wastewater treatment plants (MWWTPs) use activated sludge treatment as a secondary treatment step to remove organics, suspensions, and nutrients, but are inefficient at removing refractory contaminants such as pharmaceuticals and personal care compounds, endocrine disruptors, pesticides, additives, and microplastics, as well as their degradation intermediates [1,2]. Exposure to such organic compounds has been proven to negatively affect both human and living organisms. Even if complex organic compounds are difficult to degrade using conventional biological methods, advanced oxidation processes such as photocatalysis are capable of removing them relatively easily. The photocatalytic process involves three main steps: (i) the photo generation of charge carriers, (ii) the diffusion of charge carriers to the catalyst surface, and (iii) redox reactions on the catalyst surface. Moreover, if compared with other conventional wastewater treatment methods, such as coagulation–flocculation, ion exchange, or adsorption, the process presents the advantage of being environmentally friendly due to its mineralisation capability.

On the other hand, the most advanced MWWTP uses membrane-based processes as a tertiary treatment step to achieve outflow quality indicators suitable for reuse for

various purposes [3], but faces problems related to membrane fouling and the associated decrease in membrane operational life and increase in membrane cleaning operations and costs related to its replacement. Since organic compounds are important contributors to membrane fouling, advanced oxidation processes (including heterogeneous photocatalysis) have been investigated to improve membrane separation performance and lifetime.

The coupling of membrane-based processes with heterogeneous photocatalysis (photocatalytic membrane reactors—PMRs) has proven to be an efficient and effective alternative for municipal wastewater treatment. Among the two main PMR configurations, the slurry PMR system showed promising results compared with both the PMR design with an immobilized catalyst and other tertiary treatment processes such as chlorination, constructed wetlands, microalga cultivation, ozonation, and photo-Fenton methods [4].

Several authors have investigated the coupling of membrane filtration with photocatalysis to overcome issues related to membrane fouling and the need to remove some pollutants from the permeate water [5,6]. The advantages of heterogeneous photocatalysis among other advanced oxidation processes are represented mainly by the good reaction rate and efficiencies. The most widely used photocatalyst is TiO_2 , which is chosen for its chemical inertness, low cost, availability, non-toxicity, and recyclability. However, TiO_2 photocatalyst is inactive under visible light due to its wide band gap (3.2 eV), rapid recombination of holes/electrons pairs, and limited adsorption range in visible light (only about 4% of the solar spectrum). In this context, TiO_2 doping with metals is one of the most investigated and studied methods to improve the photocatalytic activity of TiO_2 and to ensure that its adsorption spectrum shifts towards the visible domain. This approach has been proven to be a useful tool for improving the visible light response of the catalyst and can be easily implemented by using the well-known sol–gel method.

The majority of investigated PMRs operate under UV irradiation [7,8], but there are research studies aimed at testing PMRs under visible light and/or simulated solar light as a sustainable method to solve environmental problems, of which the following are mentioned: photocatalytic membrane fouling control in wastewater treatment [3]; the degradation of various organic compounds using a visible-light-driven photocatalytic membrane [9–13]; the development of new visible light active photocatalysts for the advanced degradation of refractory organic compounds from wastewater systems [14–22].

The use of solar-light-driven PMRs for the advanced removal of organic loadings may offer the advantages of using visible light as a renewable irradiation source and having an increased lifetime for the polymeric membrane, but there are relatively few studies using real wastewater, the vast majority focused on the degradation of emerging organic pollutants from synthetic solutions [3,4].

In this context, the present work attempts to investigate the performance potential of a solar-driven PMR with a suspended catalyst, using an Fe-doped TiO_2 photocatalyst and a polysulfone-based membrane, for the advanced treatment of municipal wastewater.

2. Materials and Methods

Iron-doped catalysts were synthesised via the sol–gel method (alkoxide route) using titanium isopropoxide (Sigma Aldrich Chemie GmbH, Steinheim, Germany) and FeCl_3 (Sigma Aldrich). Ethanol (Chimreactiv, Bucharest, Romania) was used as a solvent. Titanium isopropoxide was dissolved in ethanol at room temperature under continuous stirring, and then a mixture of ultrapure water and ethanol was added to perform the hydrolysis step. Afterward, the solution of FeCl_3 in ethanol was added dropwise (in small portions under vigorous stirring). Resulted solutions were maintained under vigorous stirring for 3 h at room temperature. The resulting sols were converted into gels by drying at 80 °C for 24 h [23,24], and then thermally treated at 300 °C (catalyst sample FT1) and 400 °C (catalyst sample FT2) for 2 h. Titanium dioxide anatase form (Merck, Darmstadt, Germany) was used as a reference for the assessment of prepared catalyst photocatalytic activity.

The polysulfone-based membrane was prepared via a phase inversion process, an immersion precipitation technique using polysulfone (Psf) $M_w = 35,000$ g/mol (Sigma

Aldrich) as the base polymer, and 1-methyl-2-pyrrolidone (NMP), purity >99.5% (Merck), as a solvent. Polyvinylpyrrolidone (PVP) K30 (40,000 g/mol) (Fluka, Paris, France) and polyethylene glycol (PEG) 400, Mw = 3500–4000 g/mol (Scharlau, Hamburg, Germany) were used as additives [25]. Ultrapure water was obtained using Milli-Q Integral 15 (Merck, Millipore, Darmstadt, Germany) equipment and was used as a non-solvent in the coagulation bath. Then, 96% purity ethanol (Chimreactiv) and 99.5% glycerine (Chempur, Karlsruhe, Germany) were selected for the post-treatment and conditioning of the membranes. The membrane was obtained as follows: Psf and additives were dissolved in NMP under continuous stirring (at room temperature, for 24 h); the polymeric solution was cast onto a flat glass sheet using a “doctor blade” device with a 300 μm slot (speed 1 m/min); the casted membrane was immersed in an ultrapure water coagulation bath (for 5 min); the resulting membrane was repeatedly washed with ultrapure water and subjected to conditioning (using a 10% ethanol solution); membranes were stored in 10% glycerine solution and, prior to use, were immersed in 10% ethanol solutions for 2 h and repeatedly washed with ultrapure water.

A scanning electron microscope, FEI Quanta FEG 250 (Thermo Fischer, Waltham, MA, USA), was used for morphological characterisation and EDX (energy dispersive X-ray spectroscopy) analyses. Dimensional analysis was performed using Mastersizer 2000 (Malvern, Malvern, UK) equipment, which provides a comprehensive report of sample data on particle size distribution, specific surface area, surface-weighted mean, and volume-weighted mean. X-ray Fluorescence analyses were conducted using an X-ray fluorescence spectrometer Rigaku NEX CG EDXRF (Applied Rigaku Technologies Inc., Cedar Park, TX, USA).

The X-ray diffraction (XRD) technique was applied for the microstructural analysis of the catalyst samples. The samples studied were ground to powder form and then placed in the standard quartz trays of the diffractometer. Data acquisition was performed with the Ultima IV diffractometer (Rigaku, Tokyo, Japan) using monochromatic Cu K α radiation ($\lambda = 1.54056 \text{ \AA}$) from a fixed anode X-ray tube operated at a voltage of 40 kV and a current of 30 mA. Diffractograms were recorded for the angular 2-theta range of 10–90 degrees, in Bragg–Brentano geometry, in continuous scan mode, at a speed of 1 degree/minute, with a step width of 0.02 degrees. The crystal microstructure analysis was performed using the functionalities of PDXL software version 2.2. and ICDD database PDF4+ version 2022.

Complementary techniques of Fourier transform infrared spectroscopy (FTIR) and Raman spectroscopy were used to evaluate the changes in the molecular structures of the studied TiO₂-based as-synthesised catalysts, and these were compared with the control sample of TiO₂ anatase. Infrared spectra were recorded on a Vertex 80 infrared spectrometer (Bruker, Ettlingen, Germany) in the wave number range from 4000 cm^{-1} to 400 cm^{-1} , with 32 scans per sample and a resolution of 4 cm^{-1} . Measurements were performed in reflectance mode, using the automated total reflectance (ATR) instrumentation of the spectrometer, and powder samples were scanned without further preparation. Raman spectra were recorded at 1064 nm on a Xantus 2 spectrometer (Rigaku, Tokyo, Japan) in the wavelength range of 200–2000 cm^{-1} with a spectral resolution of 7–10 cm^{-1} . The total exposure time to collect the Raman spectra was 2500 milliseconds, and the applied laser power was 50 mW. The instrument was calibrated with pure benzonitrile before each set of measurements. Triplicate powder samples were scanned, and the average Raman spectra were taken as the result for further comparisons.

An LED lamp with 35 W power consumption, a wavelength of 380–800 nm, and a luminous flow of 1000 lumens was used to simulate solar radiation. Provided light irradiance ($\mu\text{mol}/\text{m}^2/\text{s}$) was measured with a full-spectrum meter, Apogee MQ 500 (Apogee Instruments, Logan, UT, USA). The tests were performed during the winter period, with a mean daylight irradiance below 500 $\mu\text{mol}/\text{m}^2/\text{s}$. In the case of photo degradation tests carried out under simulated solar light, the light irradiance was adjusted to match the intensity of natural daylight.

A custom-made installation was operated for the photocatalytic degradation tests. A CPC (component parabolic collector) reactor configuration was chosen due to its advantages in terms of good degradation efficiencies and lower energy losses [3,4,10]. The installation (presented in Figure 1) consists of the following main elements:

- Four transparent PETG (polyethylene terephthalate glycol) tubes with an outer diameter of 16 mm, an inner diameter of 12 mm, and a length of 1 m. The dimensions of the tubes were chosen to give the CPC reactor a total capacity of 2 litres.
- A submerged feed/recirculation pump (with the possibility to adjust the flow). A constant recirculation flow of approximately 1 L/min was used during the degradation tests. Recirculation flow was chosen to ensure a turbulent regime within the reactor tubes.
- A portable aeration pump with a flow of 1 L/min. Aeration was operated using a 30 min ON/30 min OFF algorithm.
- A feed/recirculation vessel with a capacity of 2 L.



Figure 1. Solar photocatalytic installation used for PMR slurry photocatalytic step.

The membrane separation step was performed using a KMS Laboratory Cell—CF2 system (Koch Membranen GmbH, Rimsting, Germany) operating in tangential flow at a working pressure of 2.5 bar. The membrane module presents the following main characteristics: maximum operating volume: 600 mL; minimum operating volume: 50 mL; effective membrane surface: 28 cm²; maximum operation pressure (without nitrogen pressurisation): 6 bar.

3. Results and Discussion

3.1. Photocatalyst Synthesis and Characterisation

Fe-doped TiO₂ catalysts were synthesised using a well-known sol-gel method [23,24,26,27], following the steps presented in Figure 2.

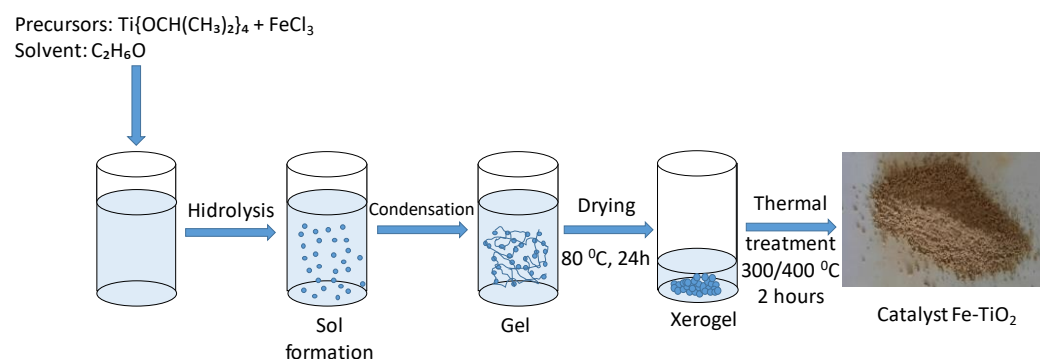


Figure 2. Synthesis of Fe-TiO₂ catalysts.

3.1.1. Scanning Electron Microscopy (SEM)

Morphological analysis of the catalyst powders revealed that the FT1 catalyst presents dimensions varying between 130 and 200 nm and that the FT2 particles have dimensions in the range of 80–135 nm (Figure 3). These results agree with the outcomes of other studies, which have shown that increasing the thermal treatment temperature results in smaller particle dimensions [23,26,27].

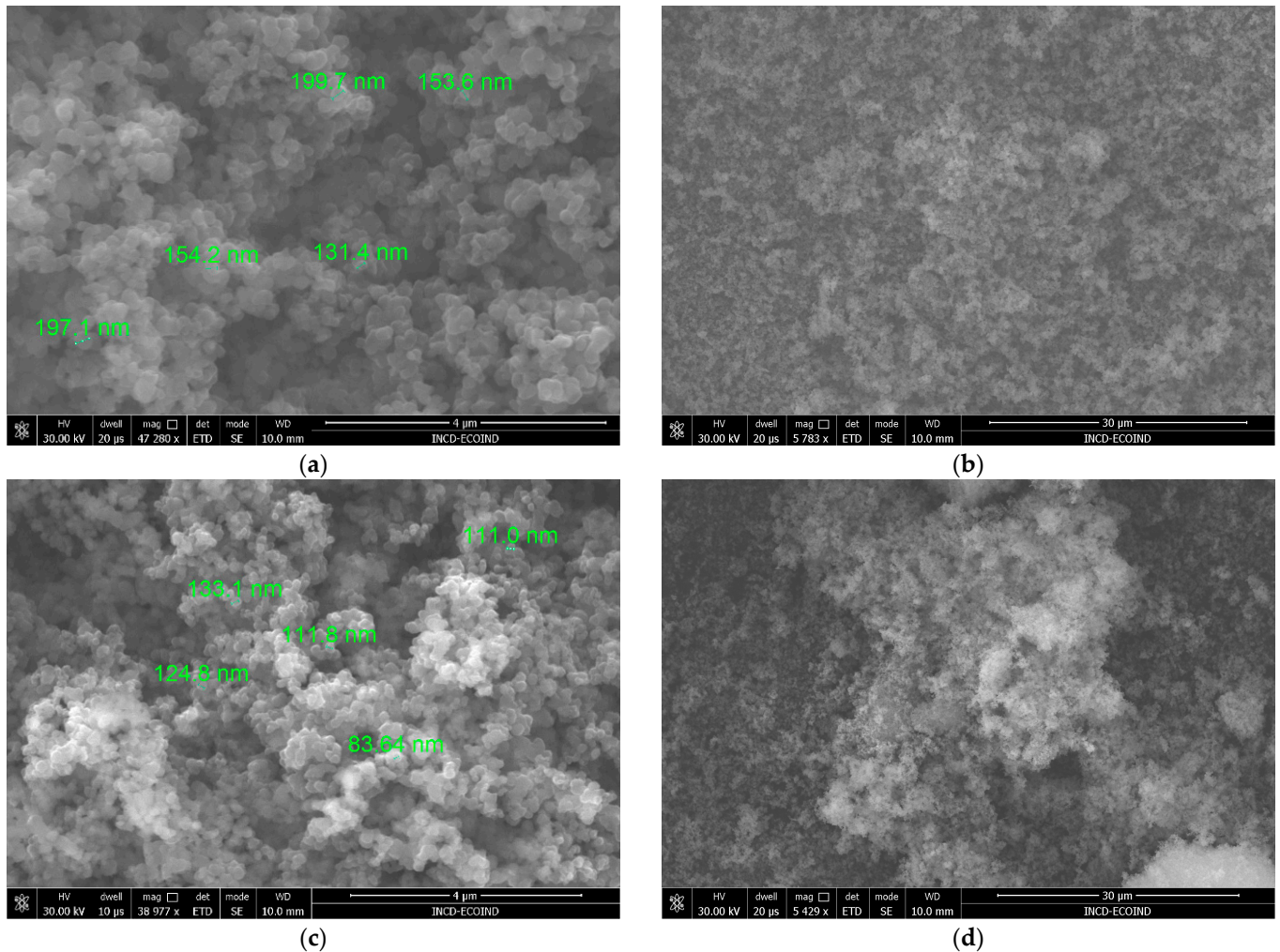


Figure 3. SEM images taken for prepared Fe–TiO₂ catalysts: FT1 at a 4 μm (a) and 30 μm scale (b); FT2 at a 4 μm (c) and 30 μm scale (d).

3.1.2. Dimensional Analyses of Fe–TiO₂ Catalysts

Dimensional analysis of the prepared catalyst showed that FT1 and FT2 have similar particle size distributions (Figure 4) with the following values: $d(0.1) = 177$ nm, $d(0.5) = 332$ nm, and $d(0.9) = 640$ nm for FT1, and $d(0.1) = 177$ nm, $d(0.5) = 332$ nm, and $d(0.9) = 633$ nm for FT2. On the other hand, the specific surface area is slightly higher for FT1 compared with that of FT2.

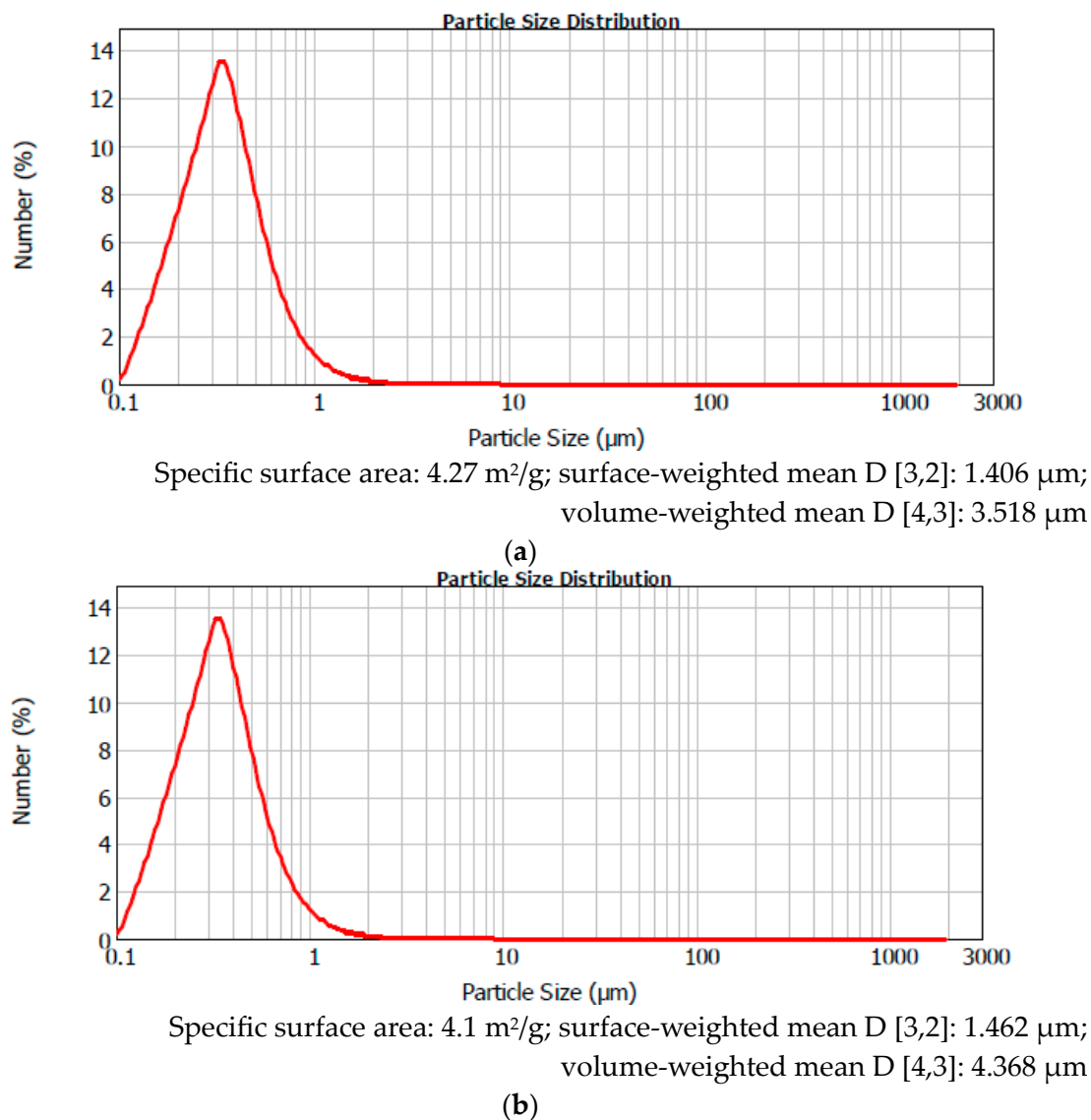


Figure 4. Dimensional analyses of (a) FT1 and (b) FT2.

3.1.3. Energy-Dispersive X-ray Spectroscopy (EDX)

EDX analysis confirmed the presence of Fe within the catalyst structure (Figure 5) with a weight percentage of about 1% compared with that of TiO₂ (see Table 1). The atomic percentages also confirm the Ti/O ratio of about 1 to 2 (Table 1).

Table 1. Prepared photocatalyst composition resulting from EDX analysis.

Element	Weight %	Atomic %
	FT1	
O K	43.91	70.16
Ti K	54.90	29.30
Fe K	1.19	0.54
	FT2	
O K	37.45	64.24
Ti K	61.68	35.34
Fe K	0.87	0.43

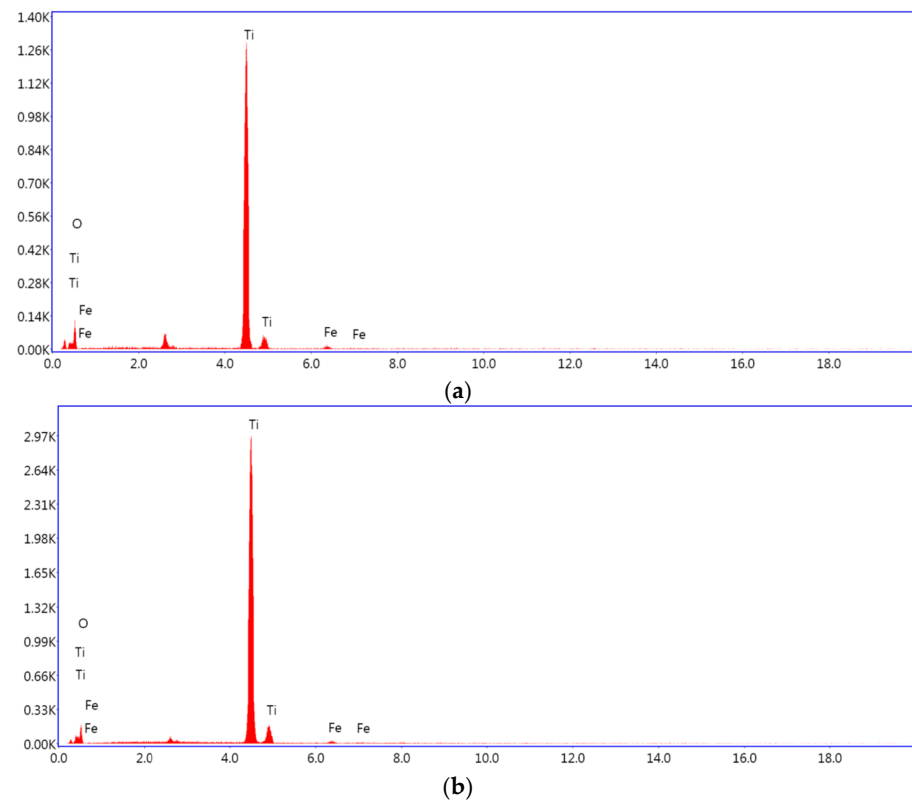


Figure 5. EDX peaks of FT1 (a) and FT2 (b).

3.1.4. X-ray Fluorescence Analyses (XRF)

X-ray fluorescence analysis also confirmed the presence of the Fe dopant in the structure of the FT1 and FT2 catalysts (see Figure 6).

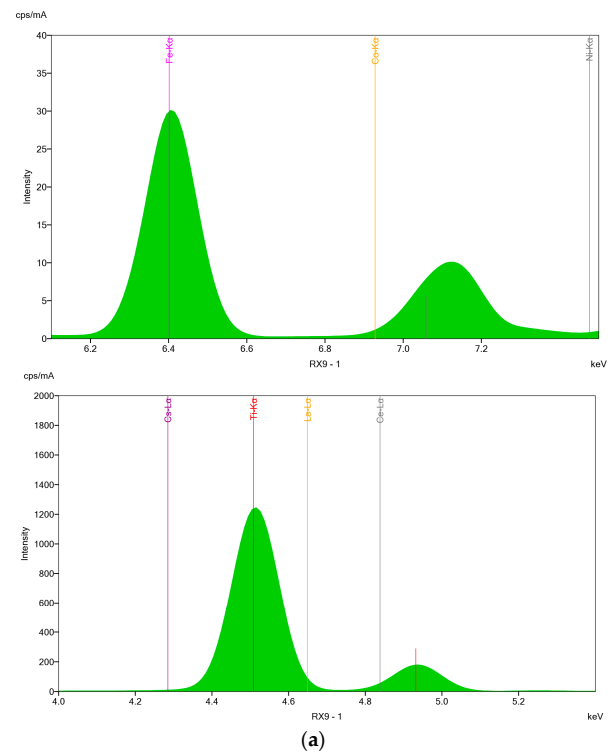


Figure 6. Cont.

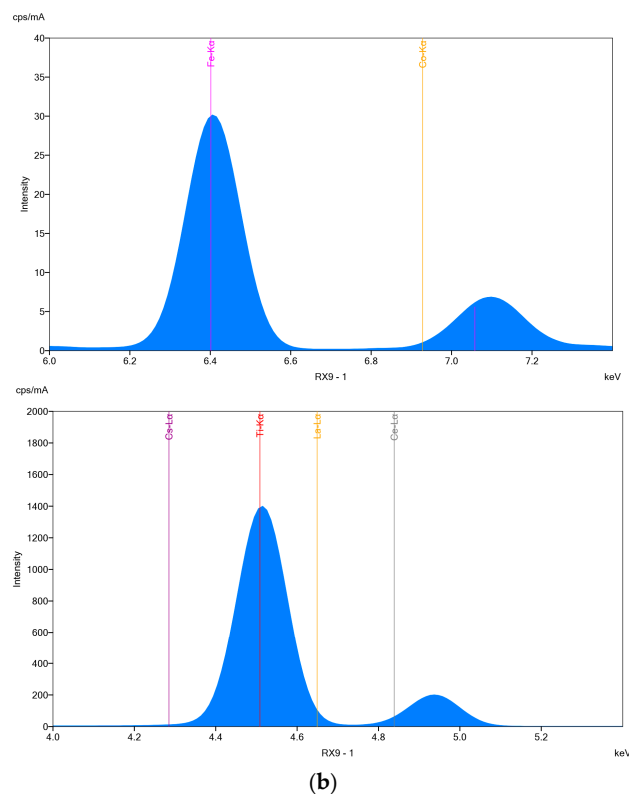


Figure 6. XRF peaks: (a) FT1; (b) FT2.

3.1.5. X-ray Diffraction (XRD)

The raw data from the XRD scans were transferred to PDXL software for Rietveld analysis. This method refines the crystal structure parameters by fitting a calculated pattern obtained from lattice parameters, crystal system, atomic coordinates, etc. to a measured diffraction pattern using the least squares method. Crystal models were built using information from ICDD, 00-064-0863 (TiO₂—anatase), and 01-079-6031 (TiO₂—rutile).

According to the shape of the X-ray patterns recorded for the catalyst (illustrated in Figure 7), it can be observed that the sample thermally treated at 300 °C seemed to develop an amorphous XRD structure. Samples with the same composition but annealed at 400 °C show a clear crystalline structure with the characteristic peaks of TiO₂ anatase at two theta values around 25, 38, 48, 54, 63, 69, 75, and 82 degrees [23,24]. Increasing the annealing temperature from 300 to 400 °C promotes crystallisation, which is reflected in the appearance of sharper and well-defined diffraction peaks. For example, the characteristic peaks (1 0 3), (0 0 4), and (1 1 2) for the anatase phase, located close to 38 degrees, can only be observed for the catalyst treated at 400 °C (FT2).

Table 2 presents the microstructural data recorded as a result of the XRD analysis of the prepared catalysts. The XRD analysis showed that the recorded diffraction peaks were assigned to the tetragonal anatase phase of titanium dioxide with the space group indicated in Table 2. This can be considered, on the one hand, as a confirmation of the TiO₂ anatase crystalline phase in all the synthesised samples, and, on the other hand, as a confirmation that, despite some microstructural changes (i.e., D spacings), the structure of the anatase titanium dioxide in the catalysts studied is maintained at both temperatures. Experiments showed a decrease in FWHM values with increasing synthesis temperature for all three peaks analysed. For instance, the FWHM value decreases from 7.41 degrees at 300 °C to 1.401 at 400 °C for the (2 0 0) peak (at 2θ of 48°), or from 5.23 degrees at 300 °C to 1.78 at 400 °C for the (0 0 4) peak. The peaks broadening correlate with crystallite dimensions below than 1000 Å.

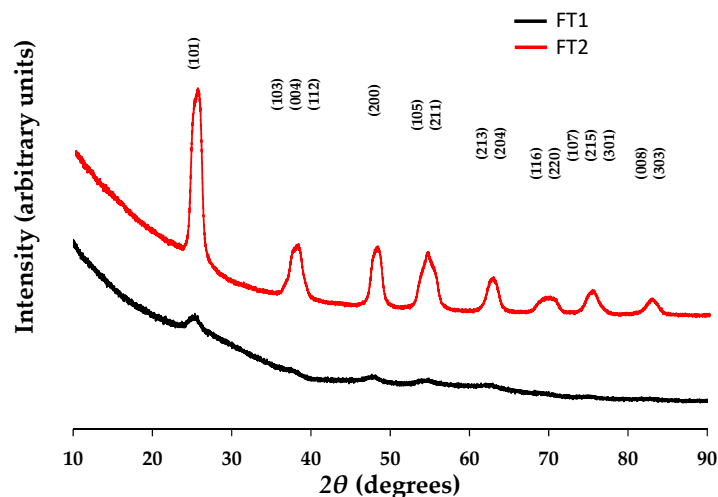


Figure 7. XRD diagram patterns recorded in Bragg–Brentano geometry for Fe–TiO₂ photocatalyst samples FT1 and FT2.

Table 2. Microstructural data for prepared catalysts.

Sample	Temp (°C)	D Spacing (Å)			Lattice Parameters			V (unit cell vol.) (Å ³)	FWHM (Degrees)			Crystallite Size, Williams–Hall Method (nm)
		(1 0 1)	(2 0 0)	(0 0 4)	a (Å)	c (Å)	Ratio c/a		(1 0 1)	(2 0 0)	(0 0 4)	
TiO ₂ anatase (PDF 00-064-0863)	235	3.51616	1.89268	2.37339	3.78536 (24)	9.4936 (7)	2.508	136.03	n/a	n/a	n/a	<100 nm
FT1	300	3.510 (4)	1.887 (4)	2.842 (6)	3.60 (8)	11.1 (3)	3.083	145 (6)	2.68 (4)	7.41 (12)	5.23 (12)	17 (4)
FT2	400	3.4833 (6)	1.8934 (3)	2.3751 (5)	3.767 (14)	9.42 (4)	2.501	133.7 (9)	0.912 (9)	1.401 (6)	1.780 (7)	69 (15)

Depending on the desired properties of the synthesised materials (i.e., catalytic activity, efficiency, etc.), this experimental finding may lead to the conclusion that the choice of thermal treatment temperature is essential to achieve the aimed functionalities. Thus, higher temperatures may result in better-organised microstructures, while lower temperatures may lead to materials with various defects (dislocations, vacancies, interstitials, substitutional, or others). It is worth mentioning that for crystallites smaller than 30 Å, the X-ray diffraction peaks become so broad and low that they are indistinguishable. However, from the perspective of ensuring the good contact of the catalyst with the reaction environment, smaller particle dimensions offer a higher contact surface, and thus synthesis at lower temperatures may be advantageous for the doped TiO₂ compositions studied in the present research. Implicitly, the synthesis procedures may be closer to green chemistry principles.

On the other hand, when looking at the crystallite size evaluated via the Williams–Hall method (full XRD patterns) in Table 2, it can be observed that the average crystallite size values for samples synthesised at 400 °C are higher than those for the same situation at 300 °C. This is evidence that a higher annealing temperature is responsible for the crystallite size increase, suggesting an increase in lattice order [23].

It is important to note that the crystallite sizes of the Fe-doped TiO₂ treated at both 300 °C and 400 °C were found to be lower than those of the commercial TiO₂ catalysts used as reference material. However, these results contradict those obtained via scanning electron microscopy.

3.1.6. Raman Spectra

The Raman spectroscopy of TiO₂ in its anatase form is a well-studied area given its significance in various applications, ranging from photocatalysis to solar cells [28].

Anatase TiO₂ is known for its distinct Raman active modes, mainly due to its tetragonal crystal structure. In pristine anatase TiO₂, the Raman spectrum typically exhibits several prominent peaks. The main peaks observed are at 399 cm⁻¹ (B_{1g} mode), 519 cm⁻¹ (A_{1g} mode), and 639 cm⁻¹ (E_g mode) (Figure 8). These modes are characteristic of the anatase phase and are related to the vibrations of the Ti–O bonds in the crystal lattice. Some changes in the Raman spectra of heated TiO₂, particularly the splitting of bands in the 200–600 cm⁻¹ region, may indicate changes in the crystal structure or the presence of defects induced by the heating process. Heating can introduce oxygen vacancies and other defect sites into the crystal lattice, changing the local symmetry and potentially leading to the splitting or shifting of Raman bands. The splitting of bands could indicate changes in the local environment around the Ti atoms, possibly due to oxygen vacancies or interstitial defects. The Raman spectra of TiO₂ can also be affected by particle size, especially as the particles approach nanoscale dimensions [28,29].

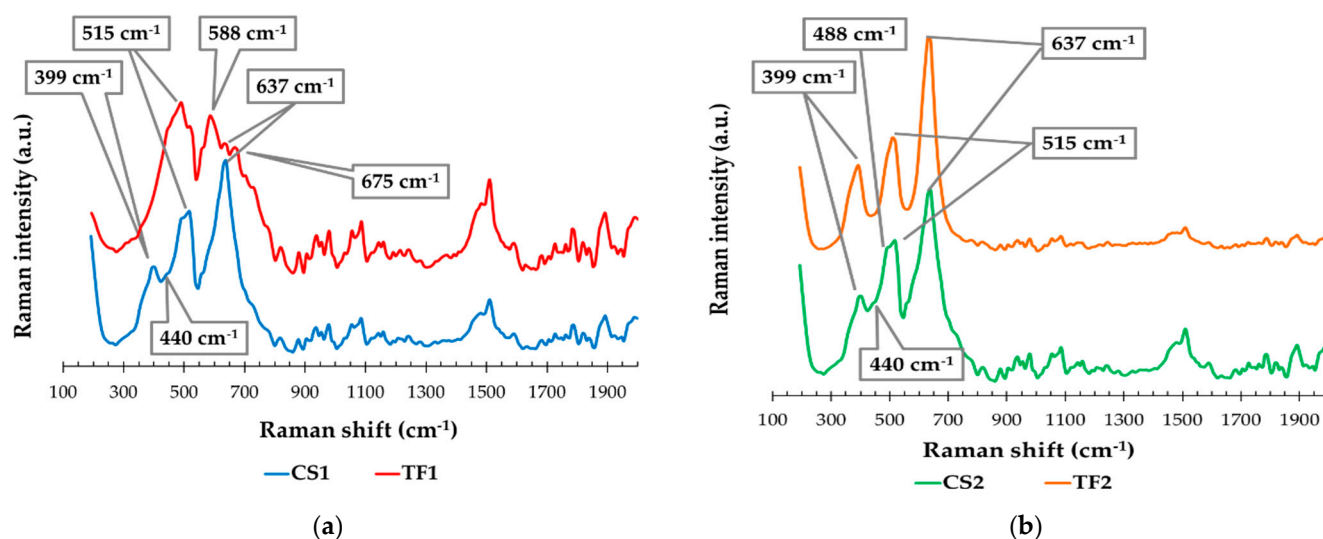


Figure 8. Raman spectra for prepared Fe-doped TiO₂ catalysts (FT) control sample-synthesised TiO₂ (CS), for the two temperatures studied: (a) 300 °C and (b) 400 °C.

In addition to the vibrations highlighted in Table 3, another peak at 488 cm⁻¹ was noted in Figure 8b, which is only observed in the Raman spectrum of the control sample TiO₂ heated to 400 °C, CS2. Moreover, the FT1 catalyst showed a distinct band at 588 cm⁻¹, which is not present in the Raman spectra of the other materials studied. This band may be related to structural defects in the material, probably caused by the presence of Fe, a phenomenon that was not recorded in the FT2 catalyst.

Table 3. Vibrational modes present in the Raman spectra of prepared Fe-doped TiO₂ catalysts (FT), and the corresponding control sample (CS), synthesised TiO₂, for the two temperatures studied, 300 °C and 400 °C (green squares confirm the band in the Raman spectra shown in Figure 8 at the indicated wavenumber).

Wavenumber (cm ⁻¹)	Sample				Vibration Modes
	CS1	CS2	FT1	FT2	
399					Anatase—B _{1g} mode (symmetric bending vibration of O-Ti-O)
440					Rutile—E _g mode (symmetric stretching vibration of O-Ti-O)
515					Anatase Ti–O A _{1g} mode (anti-symmetric bending vibration of O-Ti-O)
637					Anatase Ti–O E _g mode (symmetric stretching vibration of O-Ti-O)

3.1.7. Fourier Transform Infrared Spectroscopy

Figure 9a,b present the infrared spectra of the Fe-doped TiO₂ catalysts, FT1 and FT2, and compare them with control samples CS1 and CS2, represented by TiO₂ nano-catalysts synthesised at temperatures of 300 °C and 400 °C, respectively. In addition, the comparison includes a reference sample of TiO₂ anatase.

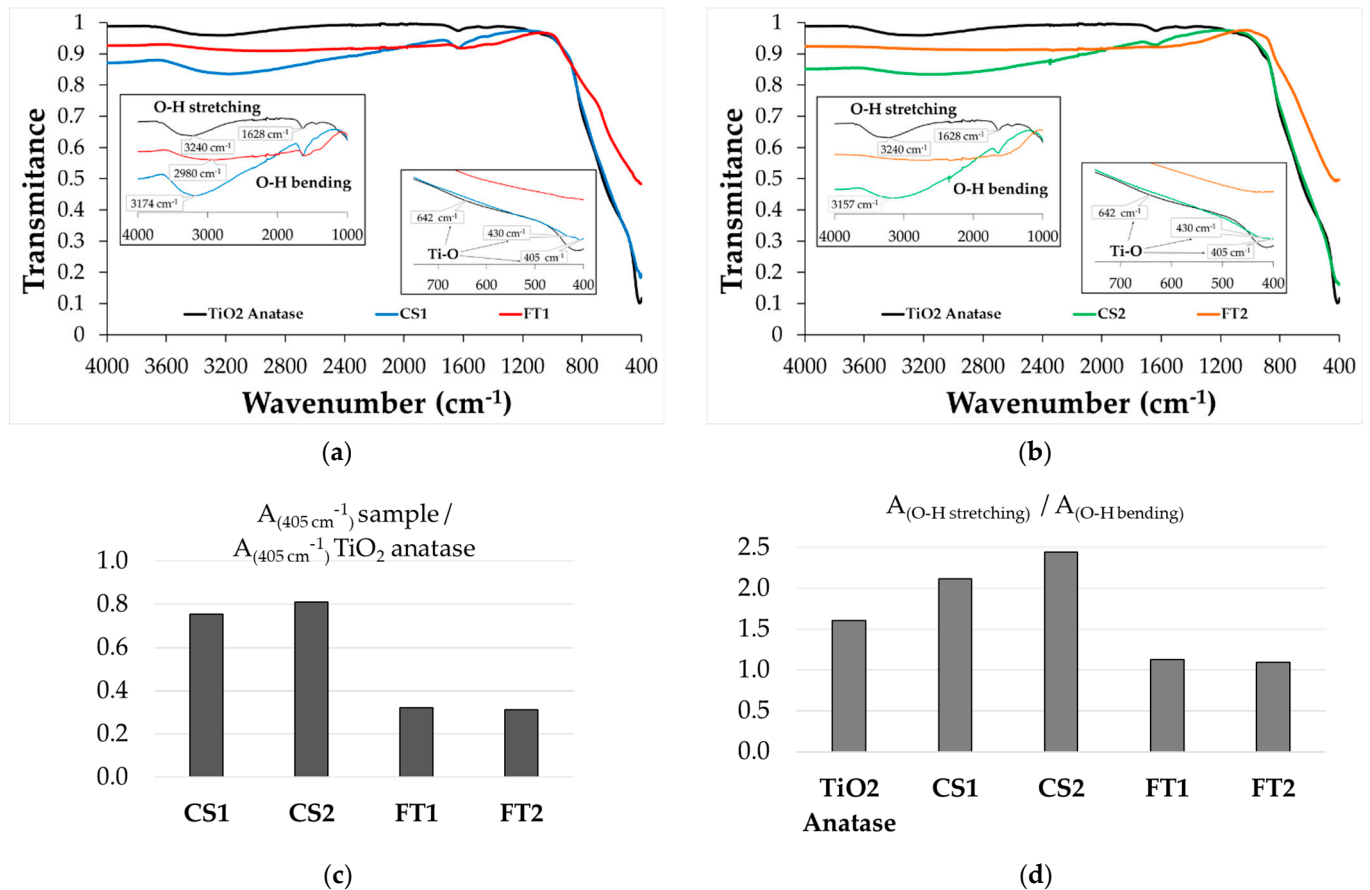


Figure 9. Infrared spectra for Fe-doped TiO₂ catalysts (FT), TiO₂ control samples (CS), and reference TiO₂ anatase recorded at temperatures of 300 °C (a) and 400 °C (b); (c) absorbance ratios calculated at 405 cm⁻¹ for each sample compared with those for the reference TiO₂ anatase; (d) the ratio of absorbance at the peak of the O–H stretching band to that at the O–H bending band.

In these spectra, including details in the insets, characteristic peaks corresponding to the vibration of the Ti–O bond can be observed at 405 cm⁻¹, 430 cm⁻¹, and 642 cm⁻¹ [30]. Significant changes can also be seen in the spectra of samples FT1 and FT2. To facilitate an objective analysis of these changes, particularly for the characteristic peak at 405 cm⁻¹, absorbance values were calculated for each sample. These values were then divided against the absorbance value of the same peak in the TiO₂ anatase reference sample, resulting in the absorbance ratios, which are compared and presented in Figure 9c. The resulting outcomes indicate a significant decrease in the intensity of the vibrational arms of the Ti–O bond when Fe was added to the TiO₂ catalyst, in both cases at annealing temperatures of 300 °C and 400 °C.

Also, in Figure 9a,b, the specific peaks of the O–H stretching vibration and O–H bending vibrations can be observed at the wavenumbers indicated in the insets. Comparing the IR spectra of the CS1 and CS2 samples with those of the reference TiO₂ anatase, it can be observed that the heating of the TiO₂ catalyst samples, at both annealing temperatures studied, leads to a slight shift in the absorption maxima for the O–H characteristic peaks, together with a broadening of the band. These changes may indicate a reorganisation of the

molecular structures of the materials upon heating, with effects on the atomic arrangements and, consequently, on the number and organisation of the hydrogen bonds formed in the catalyst structures. For Fe-doped TiO₂ catalyst samples FT1 and FT2, the same effect (even stronger) of peak shifts and peak broadening can be observed for the O–H characteristic infrared peaks.

Figure 9d shows a comparison of the absorbance ratios calculated for the studied samples, reference TiO₂ anatase, control samples with TiO₂ synthesised at 300 °C and 400 °C (CS1 and CS2), and Fe-doped TiO₂ (FT1 and FT2), by dividing the O–H stretching peak wavenumber by the O–H bending vibration peak. The recorded results highlight that the absorbance ratio decreased significantly for the Fe-doped TiO₂ catalysts. This experimental observation is correlated with a visible broadening of the O–H stretching and O–H bending bands in these samples compared with the TiO₂ anatase reference.

3.2. Experimental Photodegradation Tests

The photocatalytic activity of the prepared photocatalysts was evaluated using both natural and simulated solar light and is expressed as COD removal efficiency, with organic loading analysed in accordance with the standard SR ISO 6060:1996 [31]. The presence of an iron dopant increases the photocatalytic activity of titanium dioxide.

Experimental tests were performed using real wastewater sampled from a municipal wastewater treatment plant and stored at 4 ± 1 °C until use. The initial COD of the influent wastewater was in the range of 167.2–193.6 mgO₂/L. For all tests, the irradiation period was kept constant at 7 h (from 9 a.m. to 4 p.m.). The irradiated wastewater samples were analysed for COD determination over 1 h (seven samples per degradation test). The initial photocatalyst concentration was kept constant at 100 mg/L for all degradation experiments.

Since the photocatalytic degradation of organic compounds was shown to follow a pseudo-first-order kinetic [26,27], COD degradation can be described by a first-order kinetic (Equation (1)), which can be linearised according to Equation (2):

$$[\text{COD}] = [\text{COD}]_0 \times e^{-kt} \quad (1)$$

$$\ln\left(\frac{[\text{COD}]_0}{[\text{COD}]}\right) = kt \quad (2)$$

where [COD]₀ = initial COD of the wastewater sample; [COD] = COD of the wastewater sample at a given time; k = apparent kinetic rate constant of the first order reaction model; t = reaction (irradiation) time.

The following formula was used to calculate the ultrapure water and separation flows for the membrane process:

$$J = \frac{V}{S \times T} \quad (3)$$

where J = ultrapure water flow or separation flow; V = volume of ultrapure water or wastewater sample passing through the membrane; S = effective membrane area (in this particular case = 28 cm²); T = time in which V, volume, was collected.

3.2.1. Experimental Photodegradation Tests Using Simulated Solar Light

Experiments were carried out over a period of 7 h. Samples were analysed in 1 h intervals, and the COD value of the outflow was recorded. Experiments were also performed with a commercial TiO₂ anatase form as a reference for comparison with iron-doped catalysts. The initial catalyst concentration was kept constant at 100 mg/L for all degradation tests. PPF (photosynthetic photon flux density) was monitored in half-hour intervals (presented in Figure 10). The initial COD concentration varied between 176 and 184.8 mg O₂/L.

The iron-doped catalyst thermally treated at 400 °C—FT2—proved to achieve the highest COD removal efficiency (85.71%) after 7 h of irradiation compared with the FT1 sample (annealed at 300 °C), which achieved a COD removal efficiency of 66.67% (see Table 4). Both synthesised doped catalysts exhibit higher efficiencies compared with

commercial TiO₂, for which a COD removal efficiency of only 25.00% was reached after 7 h of irradiation. The results are in good correlation with previous research on the degradation of organic compounds using Fe-doped TiO₂ catalysts [25].

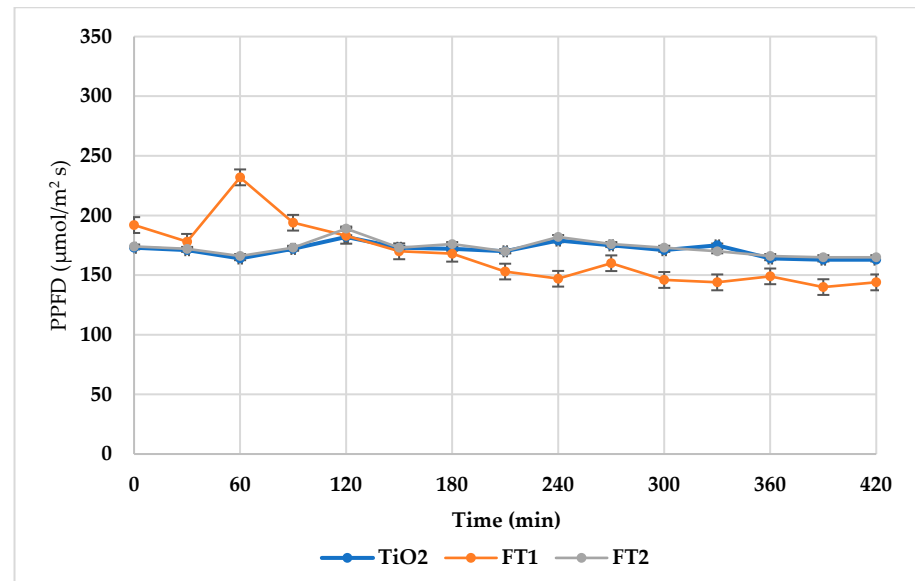


Figure 10. PPFD recorded for degradation experiments using simulated solar light.

This fact is also supported by the linearised pseudo-first-order kinetic equations concerning COD removal (presented in Figure 11). The pseudo-first-order rate constants for the simulated sunlight experiments were calculated from the slope of the linear plots (under Equations (1) and (2)) and varied in the following order: $k_{FT2} = 7.50 \times 10^{-5} \text{ s}^{-1} > k_{FT1} = 4.17 \times 10^{-5} \text{ s}^{-1} > k_{TiO2} = 1.17 \times 10^{-5} \text{ s}^{-1}$.

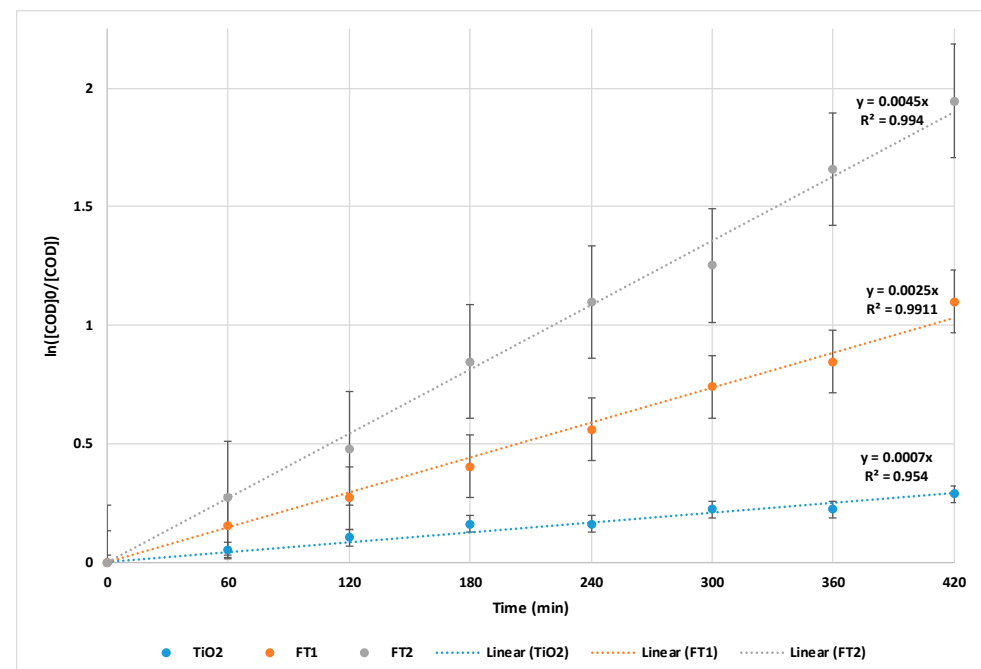


Figure 11. Pseudo-first-order kinetics of COD removal using simulated solar light.

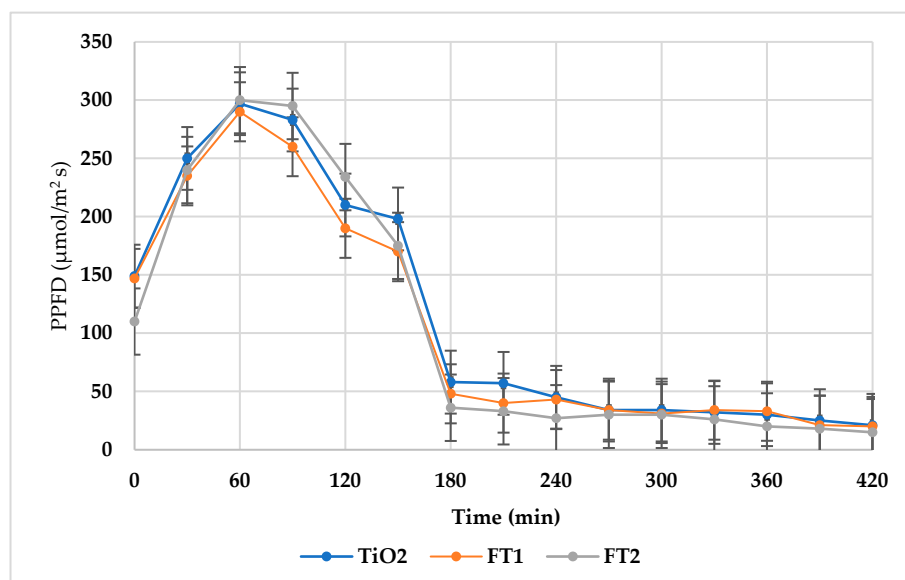
Table 4. COD removal efficiency using simulated solar light.

Time (h)	COD Removal Efficiency (%)	
	FT1	FT2
1	14.29	23.81
2	23.81	38.10
3	33.33	57.14
4	42.86	66.67
5	52.38	71.43
6	57.14	80.95
7	66.67	85.71

It can be observed that both the apparent rate constant and the degradation efficiency increase with the increase in annealing temperature from 300 to 400 °C. This behaviour can be explained by the increase in crystallite size with temperature, resulting in more active sites available for degradation.

3.2.2. Experimental Photodegradation Tests Using Natural Solar Light

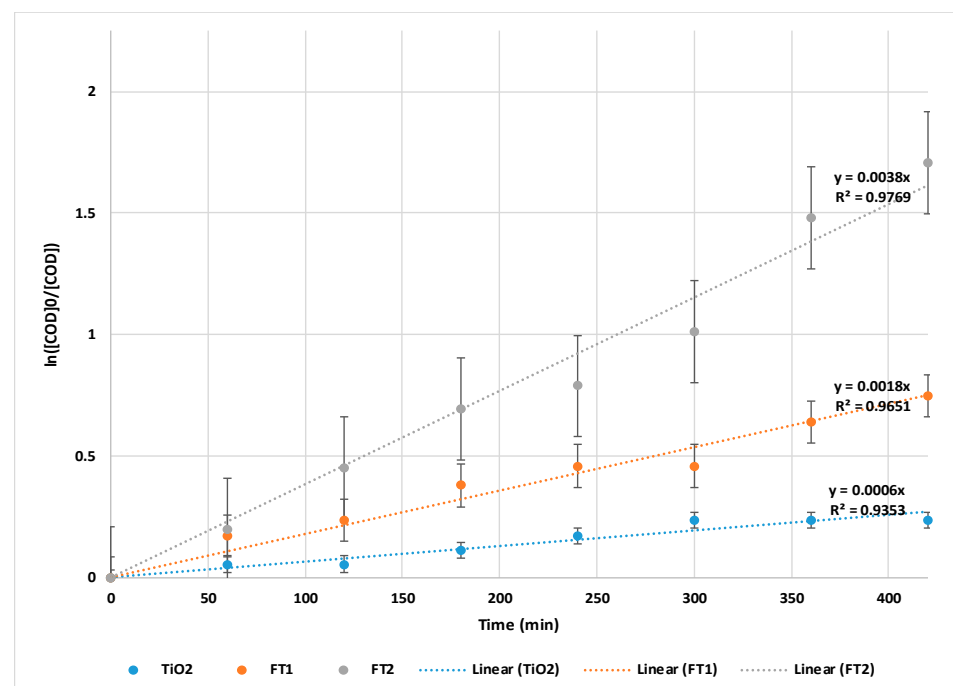
The experimental degradation tests were carried out under the same conditions as for simulated sunlight (samples analysed for COD at 1 h intervals, with an initial photocatalyst dose of 100 mg/L). As the experiments were performed in winter, the recorded PPFD varied considerably during the 7 h test period (Figure 12). However, the profile of PPFD versus time of day presented a similar pattern for all degradation tests. The initial COD concentration varied in the range 167.2–193.6 mg O₂/L.

**Figure 12.** PPFD recorded for degradation experiments using natural solar light.

The best COD removal efficiency was also achieved by the FT2 catalyst with a value of 81.82% after 7 h of irradiation (close to that obtained using simulated solar light). The FT1 catalyst led to a COD removal efficiency of up to 52.63% (Table 5), while the use of commercial TiO₂ resulted in a COD removal efficiency of only 21.05%. Linearised pseudo-first-order kinetic equations (following Equations (1) and (2)) also supported the fact that FT2 proved to be more efficient for COD removal compared with FT1 and TiO₂ (presented in Figure 13).

Table 5. COD removal efficiency using natural solar light.

Time (h)	COD Removal Efficiency (%)	
	FT1	FT2
1	15.79	18.18
2	21.05	36.36
3	31.58	50.00
4	36.84	54.55
5	36.84	63.64
6	47.37	77.27
7	52.63	81.82

**Figure 13.** Pseudo-first-order kinetic of COD removal using natural solar light.

The pseudo-first-order rate constants for the natural solar light experiments were calculated from the slope of the linear plots and were found to vary in the following order: $k_{FT2} = 6.33 \times 10^{-5} \text{ s}^{-1} > k_{FT1} = 3.00 \times 10^{-5} \text{ s}^{-1} > k_{TiO2} = 1.00 \times 10^{-5} \text{ s}^{-1}$. Similar to what was observed in the simulated solar light experiments, both the apparent rate constant and the degradation efficiency increased as the annealing temperature increased from 300 °C to 400 °C.

3.3. Overall COD Removal Efficiency of Solar PMR

The polymeric membrane used in all separation experiments was obtained from a 10% polysulfone (Psf) solution (see Figure 14).

The working pressure was maintained at 2.5 bar. All outflow volumes resulting from the photocatalytic step were subject to a membrane separation process at a concentration ratio of 1 to 2. Experimental results from the membrane separation step revealed that the membrane also acted as a barrier to organic compounds, with the overall COD removal efficiency reaching 95.24% (for the simulated solar light PMR) and 95.45% (for the solar-driven PMR), compared with 85.71% and 81.82%, respectively, when only the photocatalytic step was used. As expected, the best results were obtained for wastewater treated with the FT2 catalyst (residual COD = 8.8 mg O₂/L). The FT1 catalyst also exhibited good results in terms of COD removal, reaching efficiencies of 90.48% (for simulated solar light) and

84.21% (for the solar-driven PMR) (see Table 6). The use of commercial TiO₂ resulted in overall PMR COD removal efficiencies situated in the range of 60–64% (see Figure 15).

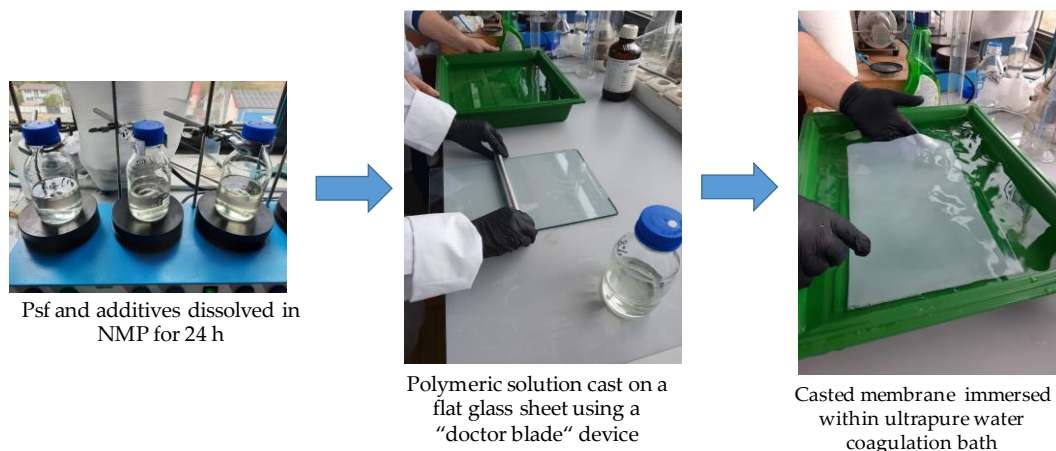


Figure 14. Preparation of 10% polysulfone membrane.

Table 6. COD removal efficiency.

Catalyst	COD Removal Efficiency (%)	
	After Photocatalytic Step	PMR Overall
	Simulated solar light	
TiO ₂	25.00	60.00
FT1	66.67	90.48
FT2	85.71	95.24
	Natural solar light	
TiO ₂	21.05	63.16
FT1	52.63	84.21
FT2	81.82	95.45

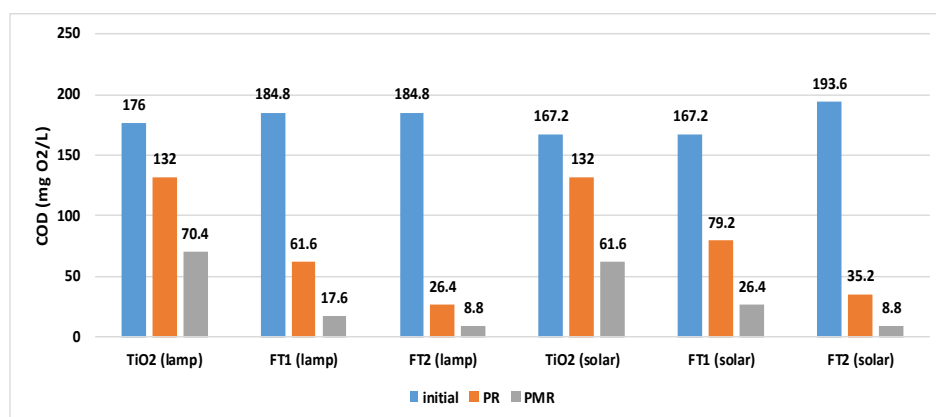


Figure 15. Total COD removal (PR—after photocatalytic step; PMR—after membrane step).

To assess membrane fouling, the ultrapure water flow rate was determined initially and after each separation flow (using Equation (3)), and the results obtained (presented in Figure 16) proved that the membrane could be used for at least six catalyst separation cycles, although membrane fouling was emphasised by the SEM images (Figure 17).

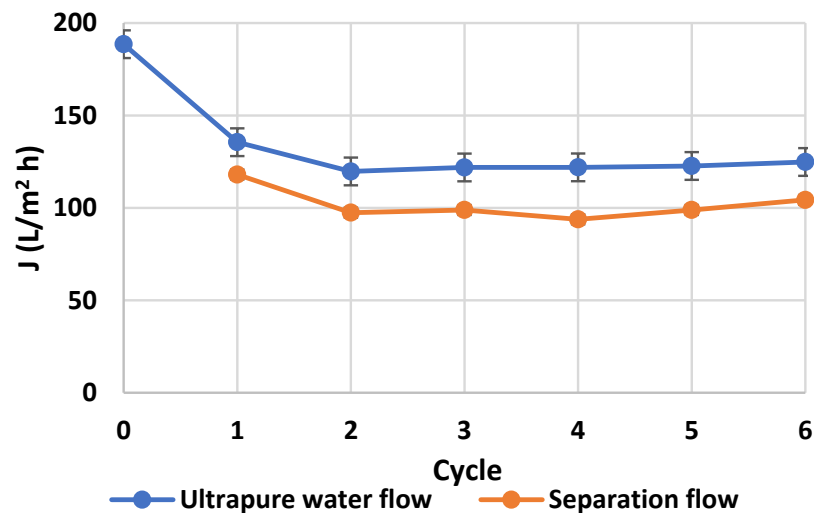


Figure 16. Ultrapure water flow and separation flow for each catalyst separation cycle.

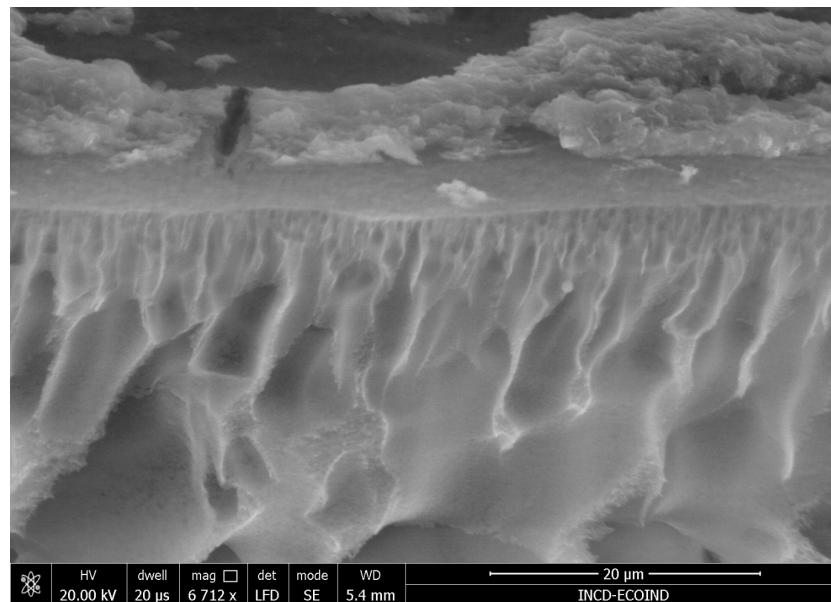


Figure 17. SEM image of 10% Psf membrane after six separation cycles.

All the ultrapure water flows determined after the separations are in the range of 115–135 L/m² h, with an overall difference of less than 16% and an average value of 124.43 L/m² h.

On the other hand, all the separation flows were determined to be between 90 and 120 L/m² h (with a total difference less than 25%; average value: 101.89 L/m² h), proving that the photocatalytic step prolongs the membrane lifetime and avoids the issues related to membrane fouling.

It should be stressed that the overall COD removal efficiency is comparable to similar results obtained for solar-driven advanced oxidation, membrane-based, or hybrid processes that can be found in the literature [3,4,31–34] (see Table 7).

Therefore, the proposed hybrid PMR system using a visible active photocatalyst in a suspension-coupled and polymeric membrane process seems to be a viable alternative for the tertiary treatment of municipal wastewater, especially when the treated effluent is intended to be reused for various purposes.

Table 7. Comparison with other studies.

Process	Results	Conditions	References
Solar photocatalysis reactor by UV, UV/H ₂ O ₂ and UV/TiO ₂	UV: TOC = 20% UV/H ₂ O ₂ : TOC = 30% UV/TiO ₂ : TOC = 50%	Reaction time = 6 h	[3]
UV-VIS photocatalytic reactor with suspended TiO ₂ for clofibric acid degradation	k = 0.00326 min ⁻¹	0.5 g/L TiO ₂ 20 mg/L clofibric acid	[4,34]
Photocatalytic ZnO foams for carbamazepine degradation	k = 0.0033 min ⁻¹	0.5 g/L ZnO 10 mg/L carbamazepine	[4,35]
Solar nanophotocatalytic pretreatment of seawater	TOC: 76.5% COD: 63.9%	2.94–3.89 mg/L TOC 4.9–5.78 mgO ₂ /L COD	[32]
Solar photo Fenton treatment of municipal wastewater	COD: 99%	Reaction time = 1.5 h 255 mg/L COD	[33]
Solar PMR for wastewater treatment	Simulated solar light: COD = 85.71%, k = 0.0045 min ⁻¹ after photocatalytic step COD = 95.24% PMR Natural solar light: COD = 81.82%, k = 0.0038 min ⁻¹ after photocatalytic step COD = 95.45% PMR	Reaction time = 7 h 100 mg/L Fe-doped TiO ₂ 167.2–193.6 mgO ₂ /L COD	This study

4. Conclusions

A solar-driven slurry PMR using Fe-doped TiO₂ photocatalysts and a 10% Psf membrane was tested for COD removal using real wastewater under both simulated and natural solar light.

Iron-doped titania catalysts were synthesised via the well-known sol-gel method and characterised via SEM, dimensional analysis, EDX, XRF, XRD, Raman spectroscopy, and FTIR. The Fe-TiO₂ photocatalyst annealed at 400 °C was found to be more efficient than the one annealed at 300 °C. Both synthesised iron-doped titania photocatalysts exhibited improved photocatalytic performance compared with that of TiO₂ for the degradation of organic compounds from real wastewater. The iron acceptance by the anatase lattice in the prepared catalysts was demonstrated by the catalyst characterisation analyses. Photodegradation experiments using real wastewater showed that the iron doping of TiO₂ resulted in a higher efficiency and rate of degradation of organic compounds compared with those for commercial TiO₂ (anatase form). A polymeric membrane was prepared using the phase inversion method, an immersion precipitation technique starting from a 10% Psf solution, and used in all separation experiments.

COD removal efficiencies reached values up to more than 95% under both simulated and natural solar light (for iron-doped titania catalyst annealed at 400 °C). The small difference between the COD removal efficiencies obtained under natural sunlight after the photocatalytic step (81.82%) compared with the COD removal efficiency obtained under simulated sunlight (85.71%) proved that solar PMRs represent a suitable alternative for the advanced removal of organic loads, especially in areas with longer daylight hours. On the other hand, the combination of solar photocatalysis with photovoltaics represents an attractive alternative to reduce process energy requirements. The photocatalytic step prevented membrane fouling after six catalyst separation cycles and also acted as a barrier to some organic compounds.

The experimental results proved that the slurry-type solar-driven PMR should be a suitable alternative for the tertiary treatment of municipal wastewater, but further tests on pilot PMR are needed to obtain data related to its sustainability compared with other

processes already used in the tertiary step of wastewater treatment (especially for visible light-driven PMRs).

Author Contributions: Conceptualisation, M.A.C., L.A.C. and O.T.; methodology, M.A.C.; investigation, C.M.N., M.B. and I.A.I.; data curation, L.A.C.; writing—original draft preparation, O.T., M.A.C. and L.A.C.; supervision, M.A.C.; writing—revision O.T., L.A.C., M.A.C., C.M.N. and M.B. All authors have read and agreed to the published version of the manuscript.

Funding: This work was carried out under the Nucleu Program within the National Research Development and Innovation Plan 2022–2027 with the support of the Romanian Ministry of Research, Innovation and Digitalisation, contract no. 3N/2022, project code: PN 23 22 03 01 and PN 23 22 04 01.

Data Availability Statement: Data will be made available on request.

Conflicts of Interest: The authors declare no conflicts of interest.

References

- García, J.; García-Galán, M.J.; Day, J.W.; Boopathy, R.; White, J.R.; Wallace, S.; Hunter, R.G. A review of emerging organic contaminants (EOCs), antibiotic resistant bacteria (ARB), and antibiotic resistance genes (ARGs) in the environment: Increasing removal with wetlands and reducing environmental impacts. *Bioresour. Technol.* **2020**, *307*, 123228. [\[CrossRef\]](#)
- Sharma, A.; Pandit, P.P.; Chopade, R.L.; Nagar, V.; Aseri, V.; Singh, A.; Awasthi, K.K.; Awasthi, G.; Sankhla, M.S. Eradication of microplastics in wastewater treatment: Overview. *Biointerface Res. Appl. Chem.* **2023**, *13*, 223.
- Ali, N.S.; Kalash, K.R.; Ahmed, A.N.; Albayati, T.M. Performance of a solar photocatalysis reactor as pretreatment for wastewater via UV, UV/TiO₂ and UV/H₂O₂ to control membrane fouling. *Sci. Rep.* **2022**, *12*, 16782. [\[CrossRef\]](#) [\[PubMed\]](#)
- Molinari, R.; Severino, A.; Lavorato, C.; Argurio, P. Which configuration of photocatalytic membrane reactors has a major potential to be used at an industrial level in tertiary sewage wastewater treatment? *Catalysts* **2023**, *13*, 1204. [\[CrossRef\]](#)
- Argurio, P.; Fontananova, E.; Molinari, R.; Drioli, E. Photocatalytic membranes in photocatalytic membrane reactors. *Processes* **2018**, *6*, 162. [\[CrossRef\]](#)
- De Filipo, G.; Pantuso, E.; Armentano, K.; Formoso, P.; Di Profio, G.; Poerio, T.; Fontananova, E.; Meringolo, C.; Mashin, A.I.; Nicoletta, F.P. Chemical vapor deposition of photocatalyst nanoparticles on PVDF membranes for advanced oxidation processes. *Membranes* **2018**, *8*, 35. [\[CrossRef\]](#)
- Khader, E.H.; Mohammed, T.J.; Albayati, T.M.; Harharah, H.N.; Amari, A.; Saady, N.M.C.; Zendejboudi, S. Current trends for wastewater treatment technologies with typical configurations of photocatalytic membrane reactor hybrid systems: A review. *Chem. Eng. Process* **2023**, *192*, 109503. [\[CrossRef\]](#)
- Szymański, K.; Grzechulska-Damszel, J.; Mozia, S. Application of a submerged photocatalytic membrane reactor with ultrafiltration membrane for ketoprofen removal during long term process: Impact of feed matrix. *J. Water Process Eng.* **2024**, *59*, 104953. [\[CrossRef\]](#)
- Roso, M.; Boaretti, C.; Bonora, R.; Modesti, M.; Lorenzetti, A. Nanostructured active media for volatile organic compounds abatement: The synergy of graphene oxide and semiconductor coupling. *Ind. Eng. Chem. Res.* **2018**, *57*, 16635–16644. [\[CrossRef\]](#)
- Zhang, Q.; Quan, X.; Wang, H.; Chen, S.; Su, Y.; Li, Z. Constructing a visible-light-driven photocatalytic membrane by g-C₃N₄ quantum dots and TiO₂ nanotube array for enhanced water treatment. *Sci. Rep.* **2017**, *7*, 3128. [\[CrossRef\]](#)
- Nguyen, T.P.; Tran, Q.B.; Ly, Q.V.; Hai, L.T.; Le, D.T.; Tran, M.B.; Ho, T.T.T.; Nguyen, X.C.; Shokouhimehr, M.; Vo, D.-V.N.; et al. Enhanced visible photocatalytic degradation of diclofenac over N-doped TiO₂ assisted with H₂O₂: A kinetic and pathway study. *Arab. J. Chem.* **2020**, *13*, 8361–8371. [\[CrossRef\]](#)
- Hu, C.; Wang, M.-S.; Chen, C.-H.; Chen, Y.-R.; Huang, P.-H.; Tung, K.-L. Phosphorus-doped g-C₃N₄ integrated photocatalytic membrane reactor for wastewater treatment. *J. Membr. Sci.* **2019**, *580*, 1–11. [\[CrossRef\]](#)
- Athanasekou, C.P.; Moustakas, N.G.; Morales-Torres, S.; Pastrana-Martínez, L.M.; Figueiredo, J.L.; Faria, J.L.; Silva, A.M.T.; Dona-Rodríguez, J.M.; Romanos, G.E.; Falaras, P. Ceramic photocatalytic membranes for water filtration under UV and visible light. *Appl. Catal. B* **2015**, *178*, 12–19. [\[CrossRef\]](#)
- Ashar, A.; Bhatti, I.A.; Ashraf, M.; Tahir, A.A.; Aziz, H.; Yousuf, M.; Ahmad, M.; Mohsin, M.; Bhutta, Z.A. Fe³⁺@ZnO/polyester based solar photocatalytic membrane reactor for abatement of RB5 dye. *J. Clean. Prod.* **2020**, *246*, 119010. [\[CrossRef\]](#)
- Sun, T.; Liu, Y.; Shen, L.; Xu, Y.; Li, R.; Huang, L.; Lin, H. Magnetic field assisted arrangement of photocatalytic TiO₂ particles on membrane surface to enhance membrane antifouling performance for water treatment. *J. Colloid Interface Sci.* **2020**, *570*, 273–285. [\[CrossRef\]](#) [\[PubMed\]](#)
- Lv, Y.; Zhang, C.; He, A.; Yang, S.-J.; Wu, G.-P.; Darling, S.B.; Xu, Z.-K. Photocatalytic nanofiltration membranes with self-cleaning properties for wastewater. *Adv. Funct. Mater.* **2017**, *27*, 1700251. [\[CrossRef\]](#)
- Liu, G.; Han, K.; Zhou, Y.; Ye, H.; Zhang, X.; Hu, J.; Li, X. Facile synthesis of highly dispersed Ag doped graphene oxide/titanate nanotubes as a visible light photocatalytic membrane for water treatment. *ACS Sustain. Chem. Eng.* **2018**, *6*, 6256–6263. [\[CrossRef\]](#)
- Alyarnezhad, S.; Marino, T.; Parsa, J.B.; Galiano, F.; Ursino, C.; Garcia, H.; Puche, M.; Figoli, A. Polyvinylidene fluoride-graphene oxide membranes for dye removal under visible light irradiation. *Polymers* **2020**, *12*, 1509. [\[CrossRef\]](#)

19. Nasseh, N.; Taghavi, L.; Barikbin, B.; Nasser, M.A. Synthesis and characterisation of a novel FeNi₃/SiO₂/CuS magnetic nanocomposite for photocatalytic degradation of tetracycline in simulated wastewater. *J. Clean. Prod.* **2018**, *179*, 42–54. [[CrossRef](#)]
20. Lin, L.; Wang, H.; Xu, P. Immobilized TiO₂-reduced graphene oxide nanocomposites on optical fibers as high performance photocatalysts for degradation of pharmaceuticals. *Chem. Eng. J.* **2017**, *310*, 389–398. [[CrossRef](#)]
21. Kamaludin, R.; Rasdi, Z.; Othman, M.H.D.; Kadir, S.H.S.A.; Nor, N.S.M.; Khan, J.; Zain, W.N.W.M.; Ismail, A.F.; Rahman, M.A.; Jaafar, J. Visible-light active photocatalytic dual layer hollow fiber (DLHF) membrane and its potential in mitigating the detrimental effects of bisphenol A in water. *Membranes* **2020**, *10*, 32. [[CrossRef](#)]
22. Nitoi, I.; Constantin, L.A.; Oancea, P.; Cristea, I.; Crisan, M. TiO₂ solar light photocatalysis a promising treatment method for wastewater with trinitrotoluene content. In Proceedings of the 15th International Multidisciplinary GeoConferences SGEM, Albena, Bulgaria, 18–24 June 2015.
23. Crişan, M.; Răileanu, M.; Drăgan, N.; Crişan, D.; Ianculescu, A.; Niţoi, I.; Oancea, P.; Şomărescu, S.; Stănică, N.; Vasile, B.; et al. Sol-gel iron-doped TiO₂ nanopowders with photocatalytic activity. *Appl. Catal. A Gen.* **2015**, *504*, 130–142. [[CrossRef](#)]
24. Vasiljevic, Z.Z.; Dojcinovic, M.P.; Vujanecic, J.D.; Jankovic-Castvan, I.; Ognjanovic, M.; Tadic, N.B.; Stojadinovic, S.; Brankovic, G.O.; Nikolic, M.V. Photocatalytic degradation of methylene blue under natural sunlight using iron titanate nanoparticles prepared by a modified sol-gel method. *R. Soc. Open Sci.* **2020**, *7*, 20078. [[CrossRef](#)] [[PubMed](#)]
25. Constantin, L.A.; Constantin, M.A.; Ionescu, I.A.; Puiu, M.D. Polysulfone and cellulose acetate-based membranes' potential application to photocatalytic membrane reactors. *Rom. J. Ecol. Environ. Chem.* **2023**, *5*, 5–16. [[CrossRef](#)]
26. Constantin, L.A.; Ionescu, I.A.; Constantin, M.A.; Stefanescu, M.; Marin, N.M. Metal-titanium dioxide doped catalysts for wastewater treatment under simulated solar light. In Proceedings of the 26th International Symposium "The Environment and the Industry" SIMI, Bucharest, Romania, 27–29 September 2023.
27. Nitoi, I.; Oancea, P.; Raileanu, M.; Crisan, M.; Constantin, L.; Cristea, I. UV-VIS photocatalytic degradation of nitrobenzene from water using heavy metal doped titania. *J. Ind. Eng. Chem.* **2015**, *21*, 677–682. [[CrossRef](#)]
28. Mohammed, S.; Elnoor, M.; Hamad, I. The Structural properties of iron oxides using Raman spectroscopy. *J. Sci. Eng. Res.* **2018**, *5*, 183–187.
29. Perevedentseva, E.; Lin, Y.-C.; Karmenyan, A.; Wu, K.-T.; Lugovtsov, A.; Shirshin, E.; Priezhev, A.; Cheng, C.-L. Raman spectroscopic study of TiO₂ nanoparticles' effects on the Hemoglobin state in individual red blood cells. *Materials* **2021**, *14*, 5920. [[CrossRef](#)]
30. Raguram, T.; Rajni, K.S. Synthesis and analysing the structural, optical, morphological, photocatalytic and magnetic properties of TiO₂ and doped (Ni and Cu) TiO₂ nanoparticles by sol-gel technique. *Appl. Phys. A* **2019**, *125*, 288. [[CrossRef](#)]
31. *SR ISO 6060*; Water Quality—Determination of the Chemical Oxygen Demand. Romanian Standards Association: Bucharest, Romania, 1996.
32. Joy, V.M.; Feroz, S.; Dutta, S. Solar nanophotocatalytic pretreatment of seawater: Process optimization and performance evaluation using response surface methodology and genetic algorithm. *Appl. Water Sci.* **2021**, *11*, 18. [[CrossRef](#)]
33. Aslam, T.; Masindi, V.; Ahmad, A.A.; Chatzisyneon, E. Valorization of acid mine drainage into an iron catalyst to initiate the solar photo-Fenton treatment of municipal wastewater. *Environments* **2023**, *10*, 132. [[CrossRef](#)]
34. Manaserro, A.; Satuf, M.L.; Alfano, O.M. Photocatalytic reactors with suspended and immobilised TiO₂: Comparative efficiency evaluation. *Chem. Eng. J.* **2017**, *326*, 29–36. [[CrossRef](#)]
35. Tasso Guaraldo, T.; Wenk, J.; Mattia, D. Photocatalytic ZnO foams for micropollutant degradation. *Adv. Sustain. Syst.* **2021**, *5*, 2000208. [[CrossRef](#)]

Disclaimer/Publisher's Note: The statements, opinions and data contained in all publications are solely those of the individual author(s) and contributor(s) and not of MDPI and/or the editor(s). MDPI and/or the editor(s) disclaim responsibility for any injury to people or property resulting from any ideas, methods, instructions or products referred to in the content.